Highlights

A practical moving Gaussian temperature boundary condition for improving melt-pool width prediction in laser powder bed fusion CFD simulations

Jun Katagiri,Sukeharu Nomoto,Masahiro Kusano,Makoto Watanabe

- A moving Gaussian temperature boundary condition modelled plume heating.
- The proposed condition improved agreement in melt pool width.
- The added boundary heating had a limited effect on melt pool depth.
- Sensitivity was examined for plume radius, delay time, and peak temperature.
- Peak temperature dominated; plume radius was secondary; delay time was minor.

A practical moving Gaussian temperature boundary condition for improving melt-pool width prediction in laser powder bed fusion CFD simulations

Jun Katagiri[a,*], Sukeharu Nomoto[b], Masahiro Kusano[b] and Makoto Watanabe[b]

[a]Integrated Research Center for Resilient Infrastructure, National Institute of Advanced Industrial Science and Technology, Higashi 1-1-1, Tsukuba, 305-8567, Ibaraki, Japan

[b]Research Center for Structural Materials, National Institute for Materials Science, Sengen 1-2-1, Tsukuba, 305-0047, Ibaraki, Japan

ARTICLE INFO

Keywords:
Laser powder bed fusion
Multiphysics CFD simulation
melt pool dimension
Vapour plume
Unsteady boundary condition
Moving Gaussian distribution

ABSTRACT

This study investigates the effect of vapour plume-induced heating on melt pool dimensions in laser powder bed fusion by using multiphysics computational fluid dynamics simulations. In our previous simulations, the melt pool depth was in reasonable agreement with experiments, whereas the melt pool width tended to be underestimated. To examine whether this discrepancy can be partly attributed to additional surface heating associated with the vapour plume, a moving Gaussian temperature (MGT) boundary condition was introduced at the upper boundary of the computational domain. The simulations showed that the proposed boundary condition increased the melt pool width and improved its agreement with the experimental measurements compared with the conventional constant-temperature boundary condition, while the effect on melt pool depth remained limited. A three-parameter sensitivity analysis was further performed for the MGT parameters, R_{vp}, t_{dl}, and T_{max}, to support practical parameter setting. Within the examined parameter range, T_{max} showed the largest contribution, followed by R_{vp}, whereas the contribution of t_{dl} was comparatively limited. These results indicate that the proposed boundary condition provides a useful reduced representation of plume-induced heating for engineering-oriented melt pool simulations.

1. Introduction

Laser powder bed fusion (PBF-LM) is a metal additive manufacturing process in which defects such as keyhole pores, balling, and lack of fusion are strongly influenced by laser processing conditions, particularly laser power and scanning speed. Because defect formation is closely related to melt pool geometry, the prediction of melt pool dimensions is an important issue in process-window assessment and process optimisation [1, 2]. Although experimental process maps provide valuable information, they require substantial time and effort. For this reason, multiphysics computational fluid dynamics (CFD) simulations incorporating heat transfer, phase change, melt flow, and laser energy absorption have been widely used to analyse melt pool formation in PBF-LM.

Several previous studies have reported reasonable agreement between simulated and experimental melt pool dimensions [3, 4, 5]. In our previous simulations, however, the melt pool depth was in reasonable agreement with experiments, whereas the melt pool width tended to be underestimated [6, 7]. This discrepancy suggested that an additional heating mechanism acting near the free surface was not sufficiently represented in the conventional boundary treatment. Previous studies have indicated that high-temperature metal vapour plumes generated during laser irradiation may remain near the powder layer and interact with the surrounding thermal field [8, 9, 10, 11]. These observations motivated us to examine whether plume-induced surface heating could partly explain the underestimation of melt pool width.

Based on this background, the objective of this study is to examine the influence of plume-induced additional heating on melt pool dimensions in PBF-LM simulations. To this end, we introduce a moving Gaussian temperature (MGT) boundary condition as a phenomenological and reduced representation of vapour plume-induced surface heating. The proposed boundary condition is incorporated into a multiphysics CFD model, and its effect on melt pool

*Corresponding author
j-katagiri@aist.go.jp (J. Katagiri)
ORCID(s): 0000-0002-6399-1951 (J. Katagiri)

dimensions is evaluated through comparison with single-track experimental data. In addition, the roles of the MGT parameters are examined to support practical parameter setting for engineering-oriented simulations.

2. Methods

2.1. Simulation overview

The simulation method is based on the general-purpose open-source CFD software OpenFOAM-8 [12, 13, 14, 15]. The details of the simulation framework used in this study can be found in our previous work [6]. A brief overview of the simulation method is given below.

The governing equations employed in the simulation are the energy equation, the continuity equation, and the Navier–Stokes equation, which are discretised within the finite-volume framework. The external force term in the Navier–Stokes equations includes surface tension represented by the continuum surface force model, recoil pressure associated with metal evaporation, and fluid-friction resistance in the solid–liquid coexistence (mushy-zone) region. The fluid is modelled as a two-phase flow consisting of metal and gas. The metal phase is treated as liquid or solid depending on temperature, and below the solidus temperature it is represented as a highly viscous pseudo-solid. The interface between the metal and gas phases is tracked using the volume-of-fluid (VOF) method. Furthermore, a ray-tracing method is employed as the heat-source model associated with laser-beam movement.

2.2. Boundary condition

In the thermal analysis, two types of boundary conditions were considered on the upper boundary in the z-direction, while the remaining boundaries were treated as adiabatic.The first was a conventional constant-temperature boundary condition in which the upper-surface temperature was fixed at 298.15 K, unless otherwise stated. The second was the moving Gaussian temperature (MGT) boundary condition proposed in this study. In the MGT condition, the vapour plume is represented as a circular high-temperature region on the upper boundary surface with a Gaussian temperature distribution. After a prescribed delay following laser movement, this temperature distribution travels at the same speed as the laser. Boundary cells outside the Gaussian temperature distribution are assigned a temperature of 298.15 K.

To maintain consistency with the OpenFOAM implementation, the MGT boundary condition was defined as a two-dimensional Gaussian distribution on the upper surface:

$$T(x, y, t) = T_0 + \left(T_{\max} - T_0\right) \exp\left[-\frac{\left(x - x_0 - V\left(t - t_{\mathrm{dl}}\right)\right)^2 + \left(y - y_0\right)^2}{R_{\mathrm{vp}}^2}\right], \tag{1}$$

where $T(x, y, t)$ is the imposed boundary temperature, T_0 is the reference temperature (298.15 K), $T_{\max}$ is the maximum temperature in the moving Gaussian distribution, (x_0, y_0) is the initial centre position of the Gaussian distribution, V is the laser scanning speed, t is time, t_{dl} is the delay time between the laser position and the plume-heating position, and R_{vp} is the characteristic radius of the plume-heating region. The detailed implementation procedure for the MGT boundary condition in OpenFOAM-8 is described in Appendix A.

Subsequent to the initiation of the calculation, a Gaussian-type temperature distribution with $T_{\max}$ as the maximum value is applied at the initial position until t_{dl} elapses. After t_{dl}, the temperature distribution moves at the laser scanning speed V. The vapour plume is an inverted cone-shaped plume formed by upward ejection of evaporated metal [16, 9, 10]. In the present study, the MGT condition was treated as a reduced and phenomenological representation of plume-induced surface heating rather than a first-principles plume model.

Because the MGT condition contains three free parameters, R_{vp}, t_{dl}, and $T_{\max}$, all three parameters were examined systematically in the present study. Their relative effects were assessed by a three-factor design-of-experiments (DOE) analysis, as described in Section 2.5.

The boundary conditions for flow velocity were as follows: the upper boundary in the z-direction employed the `pressureInletOutletVelocity` condition in OpenFOAM, while the other boundaries employed the slip condition. The `pressureInletOutletVelocity` condition specifies free outflow and inflow corresponding to the imposed pressure. The pressure was set to atmospheric pressure at the upper boundary in the z-direction, while zero-gradient conditions were imposed on the other boundaries.

2.3. Simulation setup and material parameters used

In this study, simulations were performed for a single-track test on a Hastelloy X plate without a powder bed. The material parameters of Hastelloy X employed in the present study are listed in Table 1.

Table 1
Material properties of Hastelloy X and simulation parameters used in this study

Property or parameter	Value [Unit]
Density of metal	8220 [kg/m^3]
Density of gas	1.176 [kg/m^3]
Solidus temperature	1533.15 [K]
Liquidus temperature	1628.15 [K]
Evaporation temperature	3100.0 [K] [17]
Thermal conductivity	46.1 [W/(m·K)]
Latent heat of fusion	276,000 [J/kg]
Latent heat of evaporation	6457,000 [J/kg] [17]
Specific heat capacity of solid phase	494 [J/(kg·K)]
Specific heat capacity of liquid phase	677 [J/(kg·K)]
Surface tension coefficient (σ)	1.2 [N/m]
Liquid viscosity (μ)	0.1 [Pa·s] [17]
Gas viscosity	1.865×10^{-5} [Pa·s]
Liquid-gas heat transfer coefficient	40 [W/(m^2·K)]
Laser diameter	80.0×10^{-6} [m]
Laser scanning speed	900 [mm/s]
Laser power	100, 180, 300 [W]

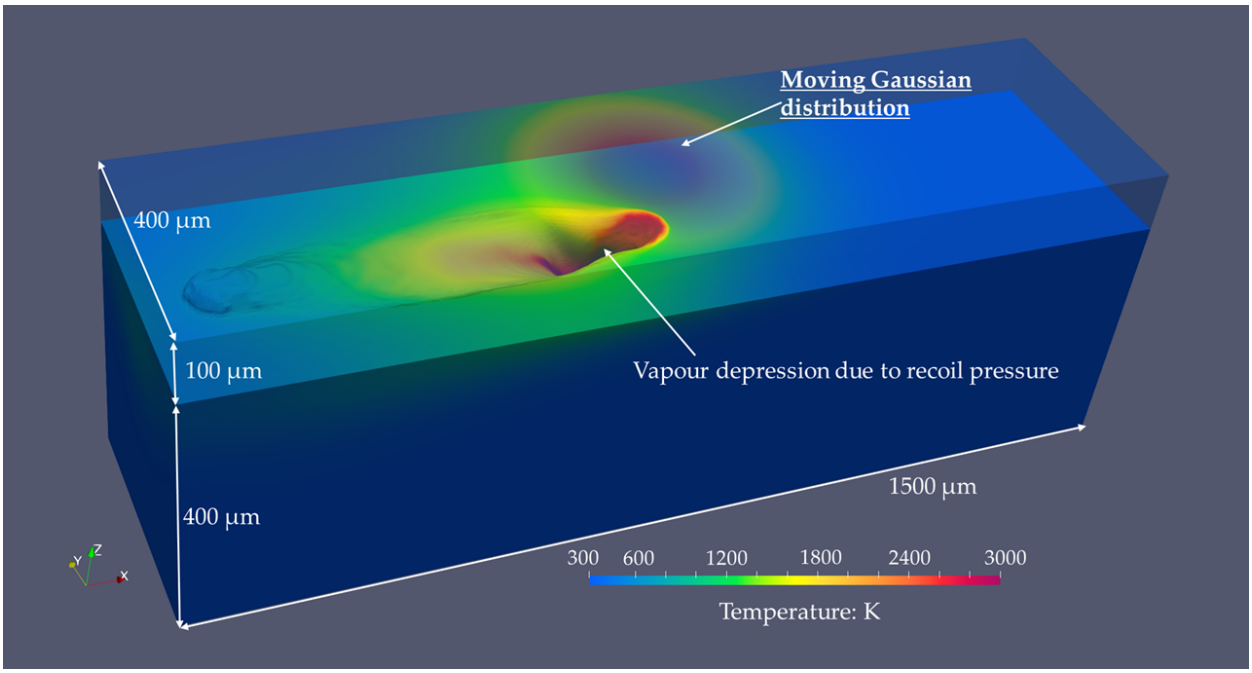

Figure 1: A snapshot of the simulation at 0.7 s

As illustrated in Figure 1, the dimensions of the simulation model were 1.5 mm, 0.4 mm, and 0.5 mm in the x-, y-, and z-directions, respectively, with a metal thickness of 0.4 mm. The grid size was set to 4 μm. The laser spot diameter was 80 μm and the scanning speed was 900 mm s^{-1}. The laser power was set to 100, 180, and 300 W. Parallel computation was performed using 96 CPU cores, and the typical computation time was approximately 24 h.

Following the simulation, ParaView (ver. 5.10.1) was used to visualise the liquidus-temperature isosurface volume. The time evolutions of the minimum and maximum coordinates in the x-, y-, and z-directions were extracted using a Python script and exported as CSV files. The melt pool dimensions were calculated as the differences between the maximum and minimum coordinates. In this study, the x-direction is defined as the melt pool length, the y-direction

as the melt pool width, and the z-direction as the melt pool depth. For quantitative comparison, melt pool dimensions were averaged over 1.0×10^{-3} to 1.4×10^{-3} s after the initial transient period, and the corresponding standard deviations over this interval were also calculated.

2.4. Experimental reference data

Experimental reference data were obtained from single-track tests conducted under the same nominal processing conditions as those used in the simulations. In the present study, the experimental melt pool width was measured from cross-sectional observations of the single tracks. The experimental values shown in the comparison figures represent the measured mean widths, and the associated error bars indicate the variability of the experimental measurements. These experimental widths were used as the primary reference for parameter selection because the conventional CFD model reproduced melt pool depth reasonably well, whereas melt pool width was systematically underestimated.

2.5. Design of experiments for MGT parameter setting

A three-factor hybrid DOE was used to examine the effects of R_{vp}, t_{dl}, and $T_{\max}$ on melt pool dimensions and to support practical parameter setting. The explored parameter ranges were $R_{\mathrm{vp}} = 5.0 \times 10^{-5}$–$3.0 \times 10^{-4}$ m, $t_{\mathrm{dl}} = 5.0 \times 10^{-6}$–$8.0 \times 10^{-5}$ s, and $T_{\max} = 1000$–6000 K. The design consisted of 45 simulation cases. It was composed of a CCD core for response-surface identification and supplementary Latin hypercube sampling points to improve coverage of the design space.

The principal response variables were the time-averaged melt pool width and depth, denoted here as W_{mean} and D_{mean}, respectively. In addition, the error relative to the experimental width and the combined error of width and depth were used as practical indicators for parameter selection.

To quantify the relative effects of the MGT parameters, a second-order response-surface model was fitted to the DOE results for each response. The following polynomial form was used:

$$Y = \beta_0 + \beta_1 R_{\mathrm{vp}} + \beta_2 t_{\mathrm{dl}} + \beta_3 T_{\max} + \beta_{11} R_{\mathrm{vp}}^2 + \beta_{22} t_{\mathrm{dl}}^2 + \beta_{33} T_{\max}^2 + \beta_{12} R_{\mathrm{vp}} t_{\mathrm{dl}} + \beta_{13} R_{\mathrm{vp}} T_{\max} + \beta_{23} t_{\mathrm{dl}} T_{\max} + \varepsilon, \quad (2)$$

where Y represents either W_{mean} or D_{mean}. Analysis of variance (ANOVA) was then performed on the fitted response-surface model. The contribution of each term was evaluated from its sum of squares and expressed as a percentage of the total modeled sum of squares, excluding the residual term. This procedure was used to identify the dominant factors and to determine whether the MGT parameters should be selected individually or in combination.

The final parameter set was selected primarily by minimising the width error relative to the experiments, while also examining the combined width–depth error and avoiding unrealistic changes in melt pool depth. In this study, the experimental melt pool width was treated as the primary calibration target, whereas the melt pool depth was used mainly as a secondary physical-consistency indicator rather than as the principal optimisation target.

3. Results and discussions

3.1. Thermal-field comparison between the MGT and constant-temperature boundary conditions

Figure 2 shows the temperature distributions at 0.8 s after the start of laser scanning for the simulation cases under the MGT condition ($R_{\mathrm{vp}} = 200$ μm, $t_{\mathrm{dl}} = 2 \times 10^{-5}$ s, $T_{\max} = 3000$ K) and the constant-temperature boundary condition. The figure shows the y–z cross-section at the centre of the x-axis, the x–z cross-section at the centre of the y-axis, and the top view of the x–y plane. The two white lines in the molten region indicate the contour lines of the solidus and liquidus temperatures, respectively.

As illustrated in the x–z and y–z cross-sections, the melt pool depth is similar under both conditions. However, under the MGT condition, the metal surface maintains a higher temperature than under the constant-temperature condition even after the laser has passed. Furthermore, the melt pool width under the MGT condition increases from the bottom toward the metal surface, whereas under the constant-temperature condition the width decreases near the surface. In addition, the rim of the melt pool under the MGT condition exhibits a slight elevation, which is not observed under the constant-temperature condition. The corresponding preliminary simulations under the constant-temperature condition, in which the imposed boundary temperature was varied from 298.15 K to 1500 K, showed that the melt pool shape became similar to that under the MGT condition when the temperature was set to 1500 K. However, in that case, the metal surface continued to melt because heating from the top surface persisted throughout the entire simulation. This result suggests that the experimentally observed melt pool shape is associated not simply with a high

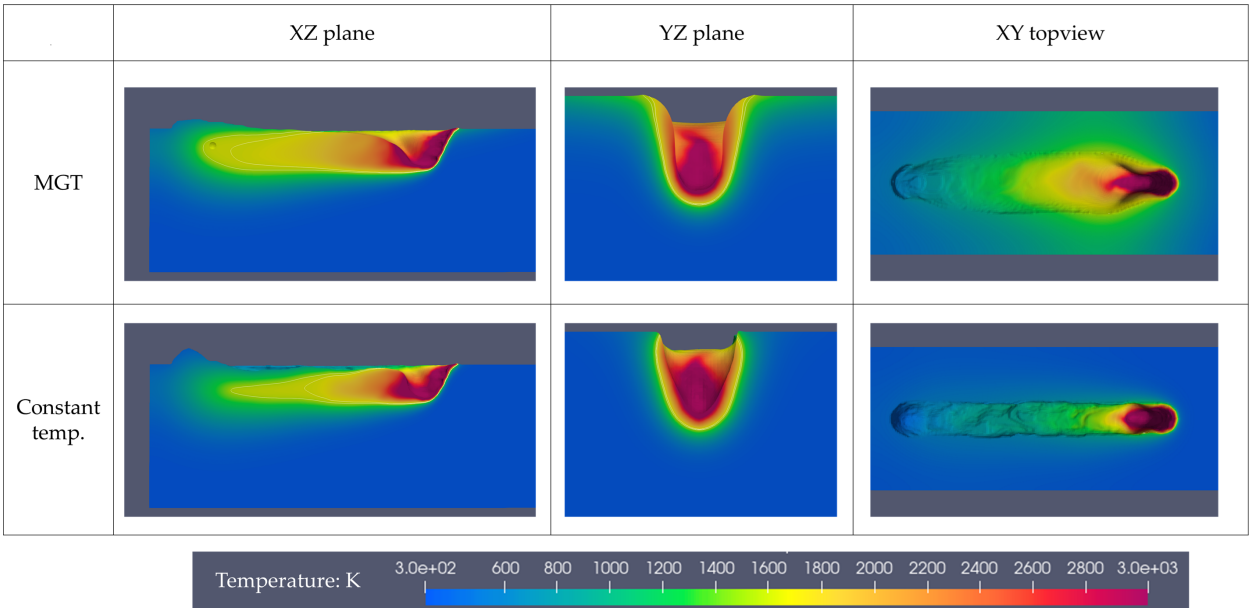

Figure 2: Temperature distributions of the simulation cases under the MGT condition and the constant-temperature condition.

boundary temperature, but with high-temperature heating acting over a limited period. In this sense, the result supports the importance of vapour plume-induced supplementary heating.

The top view in Figure 2 also demonstrates the effectiveness of the MGT condition. At the tip of the laser-induced vapour depression, the widths of the vapour depression are similar under the MGT and constant-temperature conditions. By contrast, under the MGT condition, the scanned molten line, i.e. the bead, becomes wider because the additional heat source continues to move in the wake of the laser. Moreover, under the MGT condition, molten metal accumulates in the reverse direction behind the bead, which is a feature often observed experimentally. A small amount of molten metal also accumulates and solidifies at the rear of the bead, resulting in slight erosion. The conditions considered here involve rapid cooling from several thousand Kelvin to room temperature (298.15 K), which is challenging for accurate interface tracking using the VOF method. The observed erosion is therefore attributable, at least in part, to numerical errors associated with the loss of VOF values under such severe cooling conditions. From this viewpoint, the MGT condition is also advantageous because it mitigates the rapid temperature change and improves computational stability.

The difference in melt pool length observed in the x–z view of Figure 2 is also relevant from a process perspective because melt pool length is known to be closely related to balling-type defect formation [18, 19, 20, 21, 22]. Therefore, the thermal-field difference introduced by the MGT condition is important not only for width reproduction but also for the physical interpretation of melt pool stability.

3.2. Sensitivity and ANOVA-based contribution of the MGT parameters

The comparison in Figure 2 indicates that the MGT condition qualitatively improves the thermal field and melt pool morphology. To quantify how the individual MGT parameters affect the melt pool dimensions, a DOE-based parametric analysis was conducted for R_{vp}, t_{dl}, and T_{max} using 45 simulation cases. In the following discussion, the 100 W single-track experiment is used as the reference condition. The experimental values are $W = 92.5$ μm and $D = 22.1$ μm. The DOE results showed that W ranged from approximately 77.7 to 400.0 μm. Therefore, the present parameter range provided a sufficiently wide response range for the melt pool width, including the experimental value. In contrast, D ranged from approximately 43.2 to 161.1 μm; that is, in all cases, D remained larger than the experimental value of 22.1 μm. This result suggests that, although the MGT parameters can significantly change W, reproduction of D is likely to depend on additional controlling factors.

Figure 3 shows a six-panel plot of the relationships between the MGT parameters and the melt pool dimensions. The left column shows the results for W, whereas the right column shows the results for D. In each column, the responses to R_{vp}, T_{max}, and t_{dl} are shown from top to bottom. Because interaction effects are present in the DOE, these plots should

Table 2
Representative parameter sets selected from the DOE results at 100 W.

Run ID	Criterion	R_{vp} [μm]	t_{dl} [μs]	T_{max} [K]	W [μm]	D [μm]	L [μm]
9	Min. SSE_W	50.0	42.5	3500.0	94.1	124.8	116.6
33	Min. SSE_{W+D}	118.1	31.0	1273.9	77.7	43.2	120.4

be interpreted as qualitative projections of the multidimensional response rather than as strict one-factor main-effect plots. Nevertheless, they are useful for visualising the overall direction and relative magnitude of the response changes.

For W, an overall increasing tendency was observed with increasing R_{vp} and T_{max}. In contrast, the dependence on t_{dl} was relatively weak and was mostly buried within the scatter of the results. Therefore, within the present parameter range, the dominant factors governing W can be regarded as R_{vp} and T_{max}. For D, a relatively clear increasing tendency was observed with increasing T_{max}. A moderate variation with R_{vp} was also observed, whereas the effect of t_{dl} remained limited. In other words, D was not invariant with respect to the MGT parameters and was influenced particularly by T_{max}. However, within the present parameter range, the experimental depth could not be reproduced by adjusting these parameters alone.

Figure 4 compares the percentage contributions of the response-surface terms based on ANOVA of the second-order response-surface model. The contribution of each term was calculated by normalising its sum of squares by the modelled sum of squares excluding the residual term.

For W, the linear term of T_{max} was the largest contributor, accounting for 40.8%. This was followed by the linear term of R_{vp} (27.2%) and the quadratic term of T_{max} (20.6%). The quadratic term of R_{vp} also contributed 10.6%. By contrast, the contributions of the linear and quadratic terms of t_{dl}, as well as those of the interaction terms, were very small. Therefore, the melt pool width is governed mainly by T_{max} and R_{vp}, and the response to T_{max} includes a noticeable nonlinear component. For D, the linear term of T_{max} was again the largest contributor, accounting for 56.1%, followed by the quadratic term of T_{max} at 30.1%. The quadratic term of R_{vp} contributed 5.2%, whereas the linear term of R_{vp} contributed 3.2%. The terms related to t_{dl} made only small contributions, with the largest being the $T_{max} \times t_{dl}$ interaction term at approximately 3.3%. Thus, T_{max} was also the dominant factor for D, whereas R_{vp} can be regarded as a secondary factor.

Overall, the sensitivity plots and ANOVA consistently indicate that T_{max} is the most important MGT parameter, followed by R_{vp}. The contribution of t_{dl} is comparatively small within the investigated parameter range.

3.3. Identification of parameter sets with small errors relative to the experiment

To compare the DOE results with the experimental data, the squared error for width only,

$$SSE_W = (W - W_{exp})^2 \tag{3}$$

and the combined squared error for width and depth,

$$SSE_{W+D} = (W - W_{exp})^2 + (D - D_{exp})^2 \tag{4}$$

were evaluated. The representative results are summarised in Table 2. Here, the depth response is interpreted primarily as a secondary consistency measure used to assess whether a width-improving parameter set produces an unrealistic depth prediction.

As shown in Table 2, the case that minimised SSE_W and the case that minimised SSE_{W+D} were not identical. The minimum-width-error case was run ID 9, for which $W = 94.1$ μm, i.e. very close to the experimental value of 92.5 μm. However, for the same case, $D = 124.8$ μm, which was much larger than the experimental value of 22.1 μm.

In contrast, the minimum-combined-error case was run ID 38. In this case, $D = 43.2$ μm, and the depth approached the experimental value more closely than in the other cases. However, $W = 77.7$ μm, which was smaller than the experimental width. Therefore, the condition that is optimal for width alone does not coincide with the condition that is optimal when width and depth are considered simultaneously.

This result indicates that it is not straightforward to optimise both W and D simultaneously using only a single set of MGT parameters. The present MGT representation is effective for correcting W, but it has limitations in achieving simultaneous agreement in D.

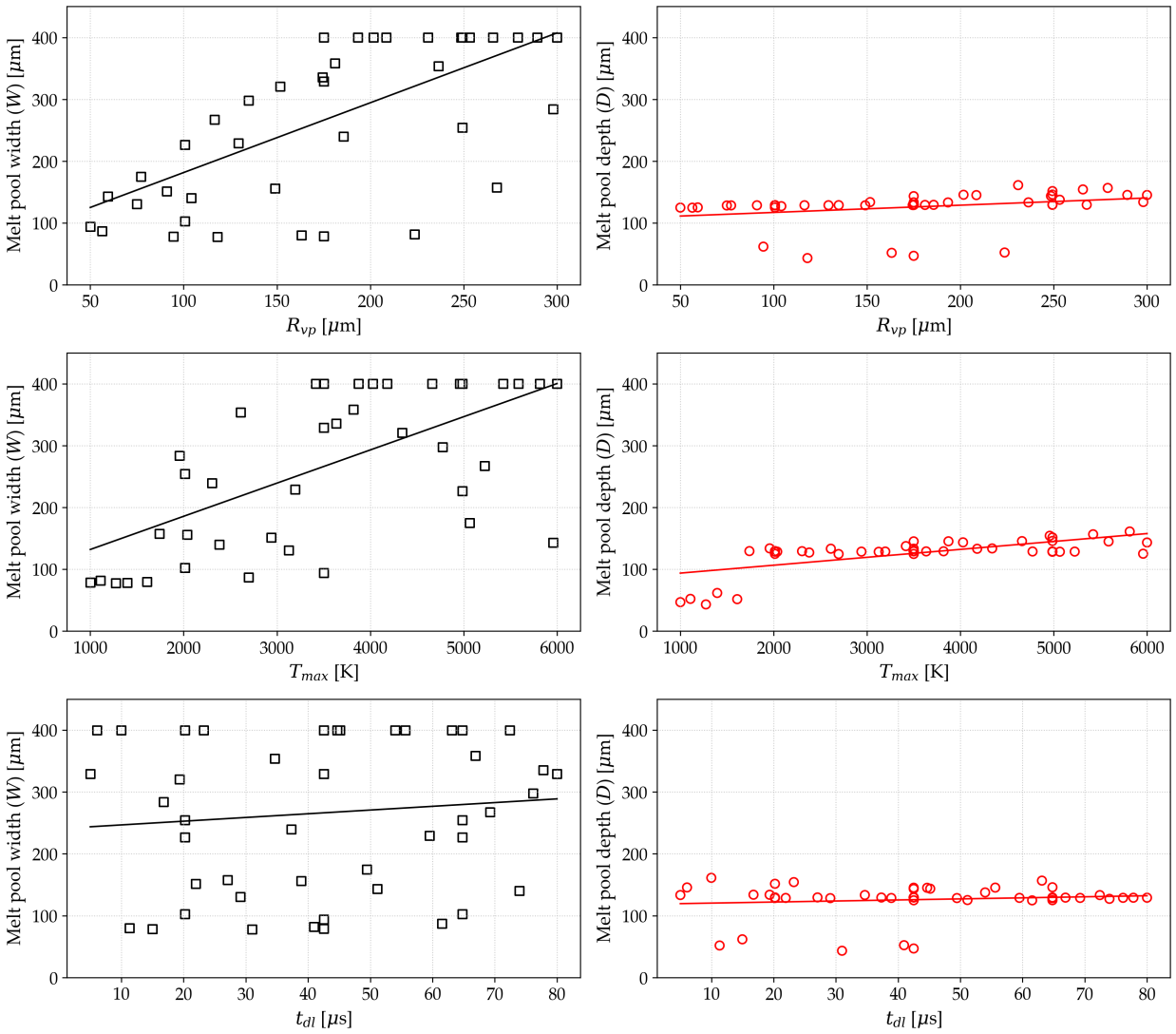

Figure 3: Relationships between the MGT parameters and the melt pool dimensions. The left column shows the melt pool width W, and the right column shows the melt pool depth D. From top to bottom, the rows correspond to R_{vp}, T_{max}, and t_{dl}.

3.4. Engineering and physical implications of the present MGT representation

The above results indicate that the present MGT boundary condition is useful primarily as an engineering parameterisation for adjusting the melt pool width W. In particular, T_{max} and R_{vp} were the major factors controlling W and were effective in bringing the simulated width closer to the experimental value.

On the other hand, although D was also influenced by T_{max}, the experimental depth could not be reproduced by adjusting the MGT parameters alone within the present parameter range. However, this does not mean that D is completely independent of the MGT representation. Rather, it suggests that adjusting only the MGT parameters does not provide sufficient degrees of freedom to reproduce the depth. In our previous study, we showed that the experimental melt pool depth could be reproduced by adjusting the absorptivity [7]. The present result is consistent with that finding. In other words, the depth depends not only on the MGT representation of plume-induced supplementary heating but also strongly on laser energy absorption. This result suggests that agreement of the depth with the experiment may require the simultaneous adjustment of both the laser absorptivity and the MGT condition.

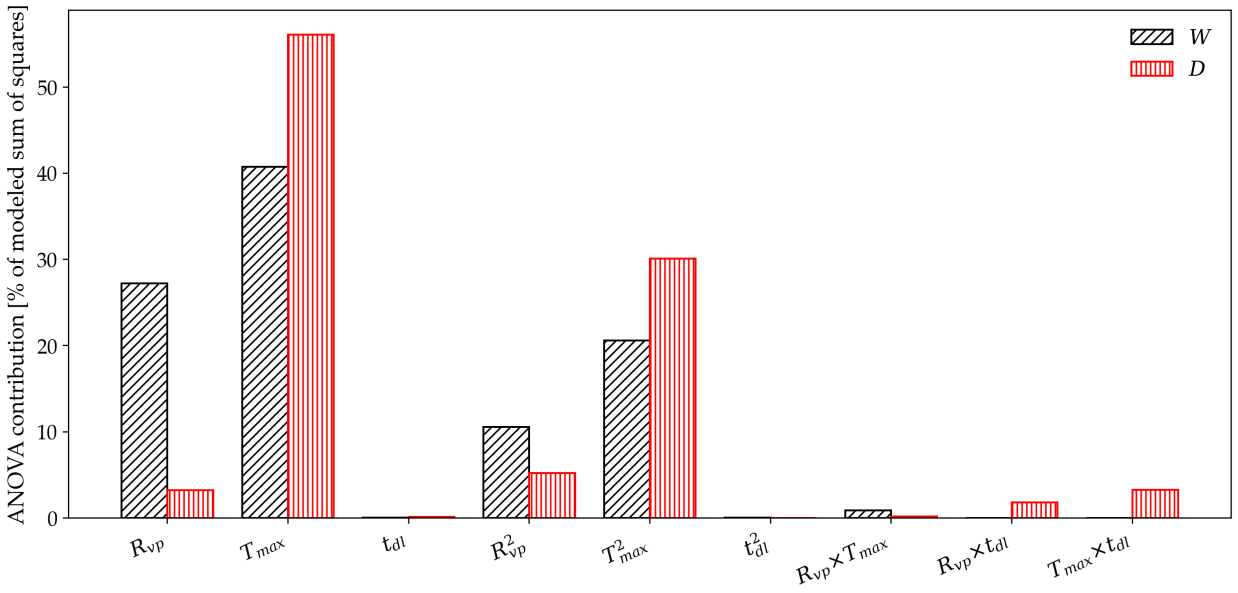

Figure 4: ANOVA-based contributions of the second-order response-surface terms to the melt pool width W and the melt pool depth D. The contributions are normalised by the modelled sum of squares excluding the residual term.

From this viewpoint, one possible reason why a relatively high absorptivity was required in our previous study is that, under the conventional boundary condition, the metal surface cooled rapidly immediately after laser passage, which may have suppressed the growth of both depth and width. In contrast, the present MGT condition leaves a high-temperature region near the surface for a certain period after laser passage, thereby representing the additional heating effect in a simple manner. This interpretation is consistent with the physical picture that the vapour plume does not instantaneously escape upward but instead remains near the metal surface for a finite time and heats the trailing region.

These considerations suggest that the assumed plume-heating distribution in the MGT boundary condition does not necessarily need to remain circular. Although it would be difficult to define a universal distribution shape applicable to all laser powers and scanning speeds, more flexible reduced representations, such as elliptical or double-ellipsoidal distributions, may improve the description of the plume-induced heating field and the resulting spatial temperature gradient and bead width [23].

In addition, the vapour plume may influence melt pool formation not only through supplementary heating but also through associated optical and multiphase effects. Previous studies have suggested possible roles of cluster formation, plume dynamics, refractive-index change, and focal shift in modifying the effective heating field and melt pool width [24, 25, 26, 27, 28]. These mechanisms are not resolved in the present model and are therefore regarded here as possible physical interpretations rather than direct conclusions. Their explicit incorporation remains a subject for future work.

Based on the above findings, a practical calibration strategy would be to first adjust the absorptivity so that the melt pool depth is approximately reproduced and then to tune the MGT parameters, especially T_{max} and R_{vp}, to match the melt pool width. Such a sequential procedure may reduce parameter non-uniqueness and clarify the respective roles of the absorptivity and the MGT parameters. In the future, further improvements in the simultaneous reproducibility of width and depth may be achieved by refining the spatial distribution shape and time-delay representation of the MGT condition.

4. Conclusions

In this study, multiphysics CFD simulations of laser scanning of a Hastelloy X plate were conducted using a moving Gaussian temperature (MGT) boundary condition to represent vapour plume-induced supplementary heating, together with a conventional constant-temperature thermal boundary condition. Quantitative comparisons were made between

the melt pool dimensions obtained from the simulations and those measured in the single-track experiments. The following findings were obtained.

- In the experiment, the melt pool exhibited a geometry in which the width expanded from the bottom toward the top surface. This geometric feature was reproduced more successfully under the MGT condition than under the constant-temperature condition. Under the constant-temperature condition, the melt pool width tended to decrease near the metal surface.
- Under the constant-temperature condition, the melt pool depth was in reasonable agreement with the experimental value, whereas the melt pool width was underestimated. By contrast, under the MGT condition, a high-temperature region remained near the top surface for a finite period after laser passage, and the melt pool width became closer to the experimental value. This result suggests that the experimentally observed melt pool shape is associated not simply with a high boundary temperature, but with supplementary heating that acts only for a limited period.
- The DOE and ANOVA results showed that, among the MGT parameters, $T_{\max}$ and R_{vp} were the dominant factors controlling the melt pool width W, whereas the contribution of t_{dl} was comparatively small. Although the melt pool depth D was also influenced by $T_{\max}$, the experimental depth could not be reproduced sufficiently by adjusting the MGT parameters alone within the investigated range. Therefore, the present MGT condition is effective primarily as an engineering parameterisation for correcting the melt pool width, whereas reproduction of the melt pool depth is likely to require additional adjustment of the absorptivity.

These results suggest that a practical calibration strategy is to first adjust the absorptivity so that the melt pool depth is approximately reproduced and then to tune the MGT parameters, especially $T_{\max}$ and R_{vp}, to match the melt pool width. Such a sequential procedure may reduce parameter non-uniqueness and clarify the respective roles of absorptivity and vapour plume-induced supplementary heating.

In the present study, the vapour plume effect was represented by a simple circular Gaussian distribution. In future work, it will be necessary to examine more flexible spatial distributions, such as elliptical or double-ellipsoidal forms, and to investigate the possible effects of plume-induced refractive-index changes and spot-size variation on melt pool formation.

A. Implementation of the MGT boundary condition in OpenFOAM

The MGT boundary condition was implemented in OpenFOAM using a `codedFixedValue` boundary condition applied to the top surface `zmax`. In the present implementation, a Gaussian temperature distribution is imposed on the top boundary after a specified delay time t_{dl}, and the centre of the Gaussian distribution moves at the same speed as the laser scanning velocity. Outside the Gaussian region, the boundary temperature is set to 298.15 K.

A typical procedure for preparing the case is as follows:

1. Copy the MGT boundary file to `0/T`.
2. Generate the mesh using `blockMesh`.
3. Initialise the case using `setFields`.

A representative example of the temperature field file is shown below. In this implementation, `scanVel`, `xini`, and `yini` define the scanning velocity and the initial position of the moving Gaussian distribution. The parameters `tref`, `Tmax`, and `Rvp` correspond to t_{dl}, $T_{\max}$, and R_{vp}, respectively.

Listing 1: Representative OpenFOAM implementation of the MGT boundary condition.

```
FoamFile
{
    version 2.0;
    format binary;
    class volScalarField;
    location "0";
    object T;
```

```
}
dimensions [0 0 0 1 0 0 0];

internalField uniform 298.15;

boundaryField
{
    xmin
    {
        type zeroGradient;
    }
    xmax
    {
        type zeroGradient;
    }
    ymin
    {
        type zeroGradient;
    }
    ymax
    {
        type zeroGradient;
    }
    zmin
    {
        type zeroGradient;
    }
    zmax
    {
        type codedFixedValue;
        value uniform 0.0;
        name vapourPlumeBC;

        code
        #{
            const fvPatch& patch = this->patch();
            const vectorField& cf = patch.Cf();
            const scalar t = this->db().time().value();

            // Laser parameters
            const scalar scanVel = 0.9;    // [m/s]
            const scalar xini    = // initial x pos. //;
            const scalar yini    = // initial y pos. //;

            // Model parameters
            const scalar tref  = 1.0e-5;    // tdl
            const scalar Tzero = 298.15;    // T0
            const scalar Tmax  = 3000.0;    // Tmax
            const scalar Rvp   = 200e-6;    // Rvp

            scalarField& field = *this;

            forAll(cf, i)
```

```
            {
                if (t >= tref)
                {
                    field[i] = Tzero + (Tmax - Tzero) *
                        exp(-1.0 *
                        (
                            pow(cf[i].x() - xini - scanVel * (t - tref), 2)
                          + pow(cf[i].y() - yini, 2)
                        ) / pow(Rvp, 2));
                }
                else
                {
                    field[i] = 298.15;
                }
            }
        #};
    }
}
```

B. Complete DOE table for the 45 simulation cases under the laser power of 100 W.

Table 3 summarises all 45 simulation cases used in the DOE for the MGT parameter study. For each case, the parameter set (R_{vp}, t_{dl}, and T_{max}) and the corresponding time-averaged melt pool dimensions (W, D, and L) are listed. The table is intended to provide the full numerical basis of the sensitivity analysis and ANOVA discussed in Section 3.2.

Table 3: DOE table for the 45 simulation cases under laser power of 100 W.

Run ID	Sampling	R_{vp} [μm]	t_{dl} [μs]	T_{max} [K]	W [μm]	D [μm]	L [μm]
1	CCD core	100.7	20.2	2013.5	102.6	128.5	133.7
2	CCD core	100.7	20.2	4986.5	226.6	128.9	303.9
3	CCD core	100.7	64.8	2013.5	102.6	125.0	139.3
4	CCD core	100.7	64.8	4986.5	226.6	128.3	284.4
5	CCD core	249.3	20.2	2013.5	254.4	129.5	267.6
6	CCD core	249.3	20.2	4986.5	400.0	151.5	975.2
7	CCD core	249.3	64.8	2013.5	254.4	129.4	257.5
8	CCD core	249.3	64.8	4986.5	400.0	145.9	903.7
9	CCD core	50.0	42.5	3500.0	94.1	124.8	116.6
10	CCD core	300.0	42.5	3500.0	400.0	145.2	774.9
11	CCD core	175.0	5.0	3500.0	329.2	133.3	431.2
12	CCD core	175.0	80.0	3500.0	329.2	129.0	402.1
13	CCD core	175.0	42.5	1000.0	78.7	46.9	119.3
14	CCD core	175.0	42.5	6000.0	400.0	143.4	716.1
15	CCD core	175.0	42.5	3500.0	329.2	129.5	412.8
16	LHS supplement	201.7	6.1	4660.4	400.0	145.6	720.7
17	LHS supplement	129.4	59.5	3195.6	229.2	128.7	250.0
18	LHS supplement	56.4	61.5	2695.6	86.9	124.7	128.4
19	LHS supplement	151.6	19.3	4340.7	320.6	133.8	438.5
20	LHS supplement	248.6	45.2	4028.7	400.0	143.6	726.7
21	LHS supplement	193.4	72.4	4180.3	400.0	133.2	536.2
22	LHS supplement	94.5	15.0	1394.9	78.1	61.7	117.3

Continued on next page

Table 3 – continued from previous page

Run ID	Sampling	R_{vp} [μm]	t_{dl} [μs]	T_{max} [K]	W [μm]	D [μm]	L [μm]
23	LHS supplement	74.9	29.1	3125.0	130.6	128.3	142.1
24	LHS supplement	236.5	34.6	2612.2	353.8	133.3	411.8
25	LHS supplement	163.2	11.3	1609.1	80.0	51.7	135.5
26	LHS supplement	298.0	16.8	1957.0	283.9	133.8	306.3
27	LHS supplement	223.7	40.9	1107.8	81.9	52.2	122.8
28	LHS supplement	181.0	66.9	3820.0	358.4	129.1	458.6
29	LHS supplement	91.0	21.9	2940.1	151.4	128.6	167.1
30	LHS supplement	134.8	76.1	4773.4	297.8	128.8	391.0
31	LHS supplement	104.1	74.0	2380.8	140.3	127.2	164.8
32	LHS supplement	77.2	49.4	5066.0	174.9	128.4	201.6
33	LHS supplement	118.1	31.0	1273.9	77.7	43.2	120.4
34	LHS supplement	267.7	27.0	1739.9	157.5	129.5	189.3
35	LHS supplement	149.1	38.9	2037.6	156.1	128.5	156.1
36	LHS supplement	278.9	63.1	5422.5	400.0	156.6	1103.6
37	LHS supplement	289.4	55.6	3872.4	400.0	145.3	828.0
38	LHS supplement	231.0	10.0	5814.5	400.0	161.1	1096.7
39	LHS supplement	59.3	51.1	5958.2	143.1	125.2	168.8
40	LHS supplement	174.5	77.8	3633.8	335.7	129.0	416.4
41	LHS supplement	208.6	44.7	5587.9	400.0	145.1	846.6
42	LHS supplement	116.5	69.3	5225.3	267.3	128.6	354.1
43	LHS supplement	253.2	54.0	3416.3	400.0	137.5	611.9
44	LHS supplement	265.7	23.2	4957.5	400.0	154.2	1029.9
45	LHS supplement	185.7	37.3	2303.6	239.7	129.3	248.4

References

[1] T. DebRoy, H. L. Wei, J. S. Zuback, T. Mukherjee, J. W. Elmer, J. O. Milewski, A. M. Beese, A. Wilson-Heid, A. De, W. Zhang, Additive manufacturing of metallic components – process, structure and properties, Progress in Materials Science 92 (2018) 112–224.

[2] R. Seede, D. Shoukr, B. Zhang, A. Whitt, S. Gibbons, P. Flater, A. Elwany, R. Arroyave, I. Karaman, An ultra-high strength martensitic steel fabricated using selective laser melting additive manufacturing: Densification, microstructure, and mechanical properties, Acta Materialia 186 (2020) 199–214.

[3] P. Ninpetch, P. Kowitwarangkul, S. Mahathanabodee, P. Chalermkarnnon, P. Rattanadecho, Computational investigation of thermal behavior and molten metal flow with moving laser heat source for selective laser melting process, Case Studies in Thermal Engineering 24 (2021).

[4] W. Alphonso, M. Baier, S. Carmignato, J. Hattel, M. Bayat, On the possibility of doing reduced order, thermo-fluid modelling of laser powder bed fusion (l-pbf) – assessment of the importance of recoil pressure and surface tension, Journal of Manufacturing Processes 94 (2023) 564–577.

[5] D. Grange, A. Queva, G. Guillemot, M. Bellet, J. D. Bartout, C. Colin, Effect of processing parameters during the laser beam melting of inconel 738: Comparison between simulated and experimental melt pool shape, Journal of Materials Processing Technology 289 (2021).

[6] J. Katagiri, M. Kusano, S. Nomoto, M. Watanabe, Influence of recoil pressure, mushy zone flow resistance and reflectivity on melt pool shape in laser powder bed fusion simulation, Case Studies in Thermal Engineering 50 (2023) 103477.

[7] J. Katagiri, S. Nomoto, M. Kusano, M. Watanabe, Particle size effect on powder packing properties and molten pool dimensions in laser powder bed fusion simulation, Journal of Manufacturing and Materials Processing 8 (2024).

[8] L. Wang, Y. Zhang, W. Yan, Evaporation model for keyhole dynamics during additive manufacturing of metal, Physical Review Applied 14 (2020).

[9] R. Wang, D. Garcia, R. R. Kamath, C. Dou, X. Ma, B. Shen, H. Choo, K. Fezzaa, H. Z. Yu, Z. Kong, In situ melt pool measurements for laser powder bed fusion using multi sensing and correlation analysis, Scientific Reports 12 (2022).

[10] I. Bitharas, N. Parab, C. Zhao, T. Sun, A. D. Rollett, A. J. Moore, The interplay between vapour, liquid, and solid phases in laser powder bed fusion, Nature Communications 13 (2022).

[11] Z. Gan, O. L. Kafka, N. Parab, C. Zhao, L. Fang, O. Heinonen, T. Sun, W. K. Liu, Universal scaling laws of keyhole stability and porosity in 3d printing of metals, Nature Communications 12 (2021).

[12] H. Versteeg, W. Malalasekera, An Introduction to Computational Fluid Dynamics: The Finite Volume Method, Pearson Education Limited, 2007. URL: https://books.google.co.jp/books?id=RvBZ-UMpGzIC.

[13] H. G. Weller, G. Tabor, H. Jasak, C. Fureby, A tensorial approach to computational continuum mechanics using object-oriented techniques, Computer in Physics 12 (1998) 620–631.

[14] J. H. Ferziger, Computational methods for fluid dynamics / J.H. Ferziger, M. Perić., Springer-Verlag, Berlin ;, 1996.

[15] T. Marić, J. Höpken, K. G. Mooney, The OpenFOAM Technology Primer, Zenodo, 2021. URL: https://doi.org/10.5281/zenodo.4630596. doi:10.5281/zenodo.4630596.
[16] H. Zheng, H. Li, L. Lang, S. Gong, Y. Ge, Effects of scan speed on vapor plume behavior and spatter generation in laser powder bed fusion additive manufacturing, Journal of Manufacturing Processes 36 (2018) 60–67.
[17] N. Afrin, P. Ji, J. K. Chen, Y. Zhang, Effects of beam size and pulse duration on the laser drilling process, American Society of Mechanical Engineers, 2016. doi:10.1115/HT2016-7339.
[18] N. K. Tolochko, S. E. Mozzharov, I. A. Yadroitsev, T. Laoui, et al, Balling processes during selective laser treatment of powders, Rapid Prototyping Journal 10 (2004) 78–87.
[19] I. Yadroitsev, P. Bertrand, I. Smurov, Parametric analysis of the selective laser melting process, Applied Surface Science 253 (2007) 8064–8069.
[20] I. Yadroitsev, I. Yadroitsava, P. Bertrand, I. Smurov, Factor analysis of selective laser melting process parameters and geometrical characteristics of synthesized single tracks, Rapid Prototyping Journal 18 (2012) 201–208.
[21] A. V. Gusarov, I. Yadroitsev, P. Bertrand, I. Smurov, Heat transfer modelling and stability analysis of selective laser melting, Applied Surface Science 254 (2007) 975–979.
[22] J. P. Kruth, L. Froyen, J. V. Vaerenbergh, P. Mercelis, M. Rombouts, B. Lauwers, Selective laser melting of iron-based powder, Journal of Materials Processing Technology 149 (2004) 616–622.
[23] J. Goldak, A. Chakravarti, M. Bibby, A new finite element model for welding heat sources, Metallurgical Transactions B 15 (1984) 299–305.
[24] E. OHMURA, I. FUKUMOTO, I. MIYAMOTO, Scattering of evaporation particles in laser ablation, Journal of the Japan Society for Precision Engineering 67 (2001) 1884–1890.
[25] J. Volpp, Impact of fume particles in the keyhole vapour, Applied Physics A: Materials Science and Processing 125 (2019).
[26] S. Chen, S. Luo, H. Yu, H. Geng, G. Xu, R. Li, Y. Tian, Effect of beam defocusing on porosity formation in laser-mig hybrid welded ta2 titanium alloy joints, Journal of Manufacturing Processes 58 (2020) 1221–1231.
[27] B. Liu, G. Fang, L. Lei, W. Liu, Experimental and numerical exploration of defocusing in laser powder bed fusion (lpbf) as an effective processing parameter, Optics and Laser Technology 149 (2022) 107846.
[28] Y. Kawahito, S. Oiwa, M. Mizutani, S. Katayama, Effects of laser-induced plume in high-power fiber laser welding with long-focal-distance focusing optics, QUARTERLY JOURNAL OF THE JAPAN WELDING SOCIETY 29 (2011) 18–23.